PHILOSOPHICAL TRANSACTIONS OF THE ROYAL SOCIETY A MATHEMATICAL, PHYSICAL & ENGINEERING SCIENCES

Transfer Processes at the Air-Sea Interface [and Discussion]

T. H. Guymer, J. A. Businger, K. B. Katsaros, W. J. Shaw, P. K. Taylor, W. G. Large, R. E. Payne, J. G. Harvey and R. T. Pollard

Phil. Trans. R. Soc. Lond. A 1983 **308**, 253-273
doi: 10.1098/rsta.1983.0003

Phil. Trans. R. Soc. Lond. A **308**, 253–273 (1983)
Printed in Great Britain

Transfer processes at the air–sea interface

By T. H. Guymer†, J. A. Businger‡, K. B. Katsaros‡, W. J. Shaw‡, P. K. Taylor†, W. G. Large§ and R. E. Payne‖

† *Institute of Oceanographic Sciences, Wormley, Godalming, Surrey GU8 5UB, U.K.*

‡ *Department of Atmospheric Sciences, University of Washington, Seattle, Washington* 98195 *U.S.A.*

§ *National Centre for Atmospheric Research, Boulder, Colorado* 80307, *U.S.A.*

‖ *Woods Hole Oceanographic Institution, Woods Hole, Massachusetts* 02543, *U.S.A.*

Near-surface data from ships, buoys, aircraft and a microwave remote-sensing satellite have been used to estimate the fluxes of momentum, heat and water vapour at the sea surface over a 200 km × 200 km area during the Joint Air–Sea Interaction Experiment of 1978. In particular, daily means of the surface heat balance and the wind stress are presented. Generally, the sensible heat flux was found to be less than 25 % of the latent heat flux. Over periods of a day the total upward heat flux was about a third of the net radiation, implying that a significant proportion of the available energy went into heating the ocean. The Ekman pumping accounted for most of the divergence in the atmospheric boundary layer but only 10 % at most of that in the upper ocean. Some case studies of the horizontal variation of the fluxes in relation to larger scales are also discussed and it is suggested that the fluxes are modulated by mesoscale patterns in sea-surface temperature.

1. Introduction

The Joint Air–Sea Interaction (JASIN) Experiment (Pollard *et al.* this symposium) is a natural link in a series of major experiments partly under GARP (Global Atmospheric Research Programme) auspices that started with BOMEX (Barbados Oceanographic and Meteorological Experiment), included GATE (GARP Atlantic Tropical Experiment) and AMTEX (Air-Mass Transformation Experiment), and, after JASIN, continued with STREX (Storm Transfer and Response Experiment). All these experiments dealt with air–sea interaction but a distinctive contribution of JASIN was the close integration of its meteorological and oceanic programmes, which facilitated the study of the turbulent fluxes and their variability in relation to the large-scale features of the mid-latitude atmosphere and ocean.

During JASIN a number of platforms carried sensors for measuring near-surface variables and sampled on scales from a few kilometres (mainly buoys), through 200 km (the separation of ships in the meteorological boundary layer programme) up to several hundred kilometres (the coverage obtained by microwave sensors on board the first satellite dedicated to oceanographic measurements, Seasat, which was operational during JASIN).

These data have been used in a number of JASIN studies, some of which are reported in this volume (Taylor *et al.*; Pollard; Prangsma *et al.*) and others of which are summarized by Pollard *et al.* (this volume). This paper concentrates on describing the measurement or estimation of surface turbulent fluxes by a variety of techniques and investigates aspects of the daily mean heat and momentum balance. It concludes with two case studies of the spatial variability of the fluxes in relation to larger scales.

2. Methods used and their accuracy

2.1. *Bulk aerodynamic formulation for surface fluxes*

One of the most common approaches to the estimation of the surface fluxes is to parametrize in terms of mean or bulk near-surface quantities as follows:

$$\left.\begin{aligned} &\tau_x = \rho C_D (u^2+v^2)^{\frac{1}{2}} u, \quad \tau_y = \rho C_D (u^2+v^2)^{\frac{1}{2}} v, \\ &u_*^2 \equiv (\tau_x^2+\tau_y^2)^{\frac{1}{2}} \rho^{-1}, \\ &E_\mathrm{h} = \rho C_P C_T |\boldsymbol{v}| (T_\mathrm{s}-T_\mathrm{a}), \quad E_\mathrm{e} = \rho L C_Q |\boldsymbol{v}| (q_\mathrm{s}-q_\mathrm{a}), \end{aligned}\right\} \tag{1}$$

where τ_x, τ_y are the components of the momentum flux, u_* is the friction velocity, E_h, E_e are the sensible and latent heat flux, u, v are the components of the wind velocity $\boldsymbol{v}$, T_a is the dry bulb temperature and q_a is the specific humidity of the air a few metres above the surface; T_s, q_s are sea-surface temperature and specific humidity, ρ is air density, C_P is the specific heat at constant pressure, and L is the latent heat of evaporation. Various determinations of the non-dimensional coefficients, C_D, C_T and C_Q, which vary both with height and stability, have been made over the years and are reviewed by Kondo (1975), Friehe & Schmitt (1976), Garratt (1977) and others. It is convenient to express them as equivalent neutral stability coefficients at 10 m. For the present study the formulations of Large & Pond (1982) have been used with

$$\left.\begin{aligned} C_{DN} &= \begin{cases} 1.14\times10^{-3}, & 3 < U_{10} < 10\,\mathrm{m\,s^{-1}}, \\ (0.49+0.065\,U_{10})\times10^{-3}, & 10 \leqslant U_{10} < 25\,\mathrm{m\,s^{-1}}, \end{cases} \\ C_{TN} &= \begin{cases} 1.13\times10^{-3}, \text{ unstable}, \\ 0.66\times10^{-3}, \text{ stable}, \end{cases} \\ C_{QN} &= 1.15\times10^{-3} \end{aligned}\right\} \tag{2}$$

(only evaluated by Large & Pond in the unstable region), where U_{10} is the wind speed at a height of 10 m.

There is still considerable uncertainty in these coefficients (at best 10 % in C_{DN}, 10 % in C_{TN} and 15 % in C_{QN}) and it is comparable with the uncertainty in the measurements of the mean quantities. The main sources of error are limited sampling, instrumentation and the effect of the sea state when it is not in equilibrium with the wind. The uncertainty is larger in C_{QN} because of difficulties associated with humidity sensors and because not many good direct humidity flux measurements are available. The effect of stability on the transfer coefficients can be accounted for, as has been shown by Deardorff (1968) and Liu *et al.* (1979). The latter also correct for the difference between interface and bulk temperature.

The mean wind and temperature data required for the bulk formulae were obtained from a number of ships and buoys. Data consist of two types: those logged manually by teams of observers on the ships, according to World Meteorological Organization (WMO) specifications, and those recorded automatically on to tape. The sampling frequency of the WMO observations varied from hourly on those vessels occupying the corners of the 200 km meteorological triangle (and on one of the ships conducting hydrographic surveys on a similar scale) to six-hourly for many of the others. Detailed cloud and wave observations were also made and three of the ships attempted rainfall measurements.

A number of the research ships and all of the meteorological buoys were equipped with

facilities for automatic logging of data. These had the advantage of providing faster sampling (frequency down to 1 per minute) but were more prone to instrumental difficulties. A particular problem was the measurement of wind direction on two of the corner ships. For the present study a subset of all the available data has been selected as indicated in table 1, locations of platforms being given in Pollard *et al.* (this symposium). Further details of the instrumentation are given in Guymer (1983), which also includes time series of the surface variables for each platform.

TABLE 1. SURFACE METEOROLOGICAL MEASUREMENTS FROM SHIPS AND BUOYS USED IN THIS STUDY

ship/buoy	sampling intervals	variables	comments
Meteor	1 h	V, p, T	R, P, P, R: manual observations according to WMO conventions
Hecla	1 h	T_w, T_s, clouds	
John Murray	1 h	waves, weather	
G. Endurer	1 h		
Tydeman	1 min	V, p, T, T_w, T_s	
Discovery	2 min	V, p, T, T_w, T_s	
W2	15 min	V, p, T, T_s	VAWR
B4	15 min	V, T, T_s	Aanderaa wind recorder

R, all surface radiation components.
P, precipitation accumulated.

An important part of the surface meteorological programme was the intercomparison of the various platforms so that systematic differences could be identified and removed. Real, spatial variations can then be examined. Three types of intercomparisons were made and have been fully reported by Guymer (1983). At the beginning and end of each observational phase the meteorological ships were positioned within 2–3 km of each other and a meteorological buoy. Winds, pressure, and air and sea temperatures were compared after allowance had been made for differences in the heights of the instruments. Several of the buoys were located within a few kilometres of each other at the southern corner of the triangle. Mean differences over successive three-day periods were calculated and it was assumed that over such a period real differences between the buoys was small. Since, R.V. *Meteor* was common to both types of intercomparison her data were used to relate the corner ships to the buoys. Finally, data obtained when R.R.S. *Discovery* and Hr. Neth. Ms. *Tydeman* passed within a few kilometres of the buoy array have also been used. Differences between the platforms were accounted for in terms of offsets, which either were present throughout all intercomparisons or could be easily correlated with other variables, e.g. overspeeding of H.M.S. *Hecla*'s anemometer. Generally, it was found that constant biases could be applied. Residual, unexplained differences were found to lie within the limits $\pm 0.7\ \mathrm{m\,s^{-1}}$ for wind speed, $\pm 5°$ for wind direction, ± 0.5 K for dry bulb, ± 0.2 K for wet bulb and ± 0.2 mbar pressure.†

For the foregoing, the vector-averaging wind recorder (VAWR) on buoy W2 has been used as an arbitrary standard to which all JASIN surface observations have been related. The problem of its absolute accuracy has been difficult to resolve. Although, the sensors provided a continuous, clean data set there were problems in wind speed measurements below $3\ \mathrm{m\,s^{-1}}$ (Guymer 1983). Weller *et al.* (1983) have investigated the instrument's behaviour using post-experiment calibrations. Their results suggest that we cannot be certain of the absolute

† bar = 10^5 Pa.

accuracy of wind speeds from the W2 VAWR to better than about 7 %. This is discussed further in § 2.3.

2.2. *Eddy correlation technique*

The eddy correlation method of calculating turbulent fluxes is difficult to use because of the combination of high frequency demands upon the instrumentation and, over the ocean, because of motion induced in surface-bound platforms. Three aircraft, which do not have the extreme motion problems of surface platforms, participated in JASIN (Nicholls *et al.* this symposium). A Falcon, a C-130 and an Electra carried turbulence probes for measuring high frequency (up to 10 Hz) fluctuations of the three wind components, temperature and humidity. The Falcon was in an early stage of development and had considerable difficulty with wind instrumentation during the experiment. The other two aircraft have well developed data acquisition systems and provided excellent stress measurements. Principles of gust-probe operation are detailed by Lenschow (1970) and Nicholls (1978). Nicholls *et al.* (1983), on the basis of thorough flux intercomparisons between the aircraft, show that the run to run variability of stress and sensible heat flux (typically ± 25 % and a few W m^{-2} respectively) is much greater than differences between the Electra and the C-130 on a given intercomparison run (< 10 % and < 1 W m^{-2}). Therefore, the accuracy of flux measurements from these platforms may be inferred to be limited by sampling rather than instrumental error.

In this paper interest in the aircraft flux data will be focused on the spatial variability of the Electra and C-130 fluxes on 1 September and on the comparison of the stress field with that measured by Seasat at about the same time. Fluxes were computed by first high-pass filtering the time series with a 5 km compound running-mean subtraction filter (Holland 1973) to remove means and non-turbulent low frequencies and then calculating desired cross products from the resulting signals.

2.3. *Dissipation method*

This method is particularly suited to shipboard operation in high winds at sea because vertical velocity measurements are not explicitly required, the ship's speed need not be removed from the relative wind speed and reasonably robust sensors will respond to the required frequencies, which are higher than wave frequencies (Large & Pond 1982). The instrumentation, which has been described by Large (1979) and Pond *et al.* (1979), consisted of a Gill propeller-vane anemometer, glass-coated microbead thermistors for fluctuating temperature and a Lyman α humidiometer to measure moisture fluctuations, and was mounted either on the boom of *Meteor* at a height of 10 m or on the mast at 22 m. Rates of molecular dissipation of kinetic energy, and of temperature and moisture variance were inferred from spectral density estimates of the downstream velocity, air temperature and absolute humidity at frequencies in the $k^{-\frac{5}{3}}$ region of the spectrum. Values of the required constants are not well established over the sea and some of the assumptions have not been tested; therefore direct comparisons with eddy correlation measurements are necessary. Large & Pond (1982) have reported such comparisons and concluded that the dissipation technique is a useful means of measuring turbulent fluxes over the deep ocean. Fluxes were computed with 20 min segments of data. Approximately 400 h of stress data were collected in JASIN. Large & Pond (1982) used these in conjunction with meteorological measurements on *Meteor* to examine the exchange coefficients C_{DN}, C_{TN} and C_{QN}, and this in part forms the basis of the formulations (2).

The momentum fluxes have been used to investigate the accuracy of W2 winds referred to since the stress is particularly sensitive to errors in the wind. Figure 1 shows the dissipation flux

plotted against bulk aerodynamic fluxes calculated from the W2 VAWR winds and separated according to whether the wind was increasing or decreasing. With increasing wind speed there is good agreement but with decreasing wind speed the W2 fluxes are systematically higher. These differences persist over periods of a day or so and may point to a sea-state dependence of the W2 winds. It should be noted that when the dissipation fluxes are compared with those inferred from the Gill anemometer during JASIN and other experiments the dependence on wind speed tendency is in the reverse sense, i.e. dissipation fluxes are higher than bulk fluxes in decreasing winds. Further work is being undertaken but the results admit the possibility that winds from the W2 VAWR are 5–10 % too high on some occasions.

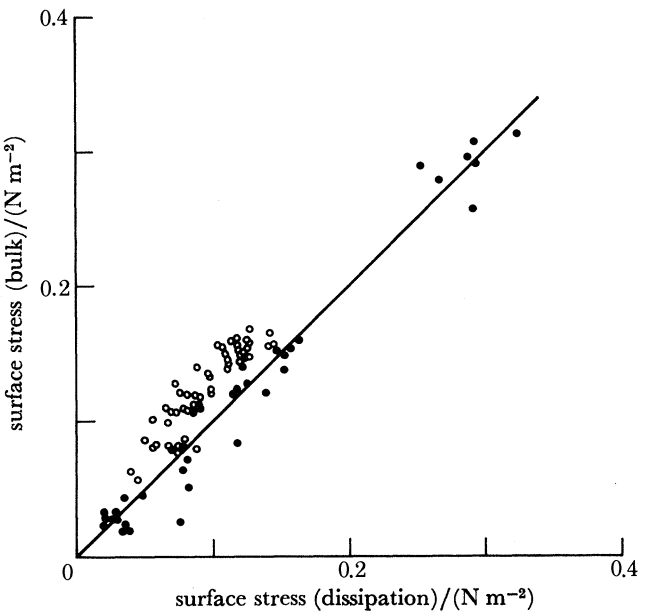

FIGURE 1. A comparison of the surface stress calculated by using the bulk parametrization method (equations (1), (2)) applied to the VAWR data on buoy W2 with values derived from dissipation measurements on *Meteor*. Full circles, increasing wind speed; open circles, decreasing wind speed.

2.4. *Seasat scatterometer*

The Seasat-A satellite scatterometer (SASS) was one of several microwave sensors on board the first oceanographic satellite (Born *et al.* 1981). Estimates of wind velocity have been made from a height of 800 km. The technique is based on the sensitivity of microwave radar backscatter to the amplitude of short (a few centimetres) gravity waves created on the sea surface by the action of the wind. The sensor and the algorithm used to convert radar backscatter into winds are described in Grantham *et al.* (1977), Johnson *et al.* (1980) and Bracalente *et al.* (1980). Wind speed and direction are averaged over resolution cells *ca.* 15 × 70 km for incidence angles between 25° and 55°, which correspond to swaths of 500 km on either side of the sub-satellite track. Although there is some hope of retrieving stress directly from the backscatter measurements (Liu & Large 1981), there are insufficient direct measurements of the stress from surface-based systems to develop a suitable algorithm. Instead, values were calculated from the scatterometer winds, which are referred to a height of 19.5 m, by using a constant flux layer model.

Because of the relatively high quality of the JASIN surface data, they were used as an independent assessment of the accuracy of the scatterometer. In a comparison of 23 passes, selected

to cover the maximum range of wind conditions Jones *et al.* (1981) found that the standard deviation of the wind speed differences was $\pm 1.6\,\mathrm{m\,s^{-1}}$ and that of direction $\pm 18°$, some of which is due to instrumental errors and unrepresentativeness of the surface data. Biases were small. One pass exhibited much larger differences than the others and an analysis of JASIN data, satellite cloud imagery and other Seasat sensors (Guymer *et al.* 1981) have shown this to be related to a thunderstorm. However, since the precipitation during the rest of JASIN was predominantly drizzle or light rain this is not considered to have a significant effect on the results presented.

2.5. *Estimation of surface radiation components*

The available surface heating as given by the net radiation and its spatial variation is an important quantity if the heating of the ocean is required. Only two of the ships, *Meteor* and M.V. *Gardline Endurer*, measured all four components of the radiation budget. However, Lind & Katsaros (1983) and Lind *et al.* (1982) have applied parametrization schemes that use the WMO cloud observations to deduce the downward shortwave and longwave components (which are the most variable) at the remaining corner of the triangle and, during phase 2, at the centre ship. The shortwave model, due to Lumb (1964), requires amount, type and height of the significant cloud groups. For the longwave component a new model was developed that also makes use of surface temperature, mixing ratio and the heights and temperatures of the 850, 700 and 500 mbar isobaric surfaces. From these it was possible to infer cloud-base temperatures. Although these formulations are crude, comparisons with the *Meteor* and *Endurer* measurements show that the error over 12 days in the shortwave component was 5 % and was less than 1 % for similar periods for the downward longwave component. The worst daily mean error in the longwave case was 3.4 % and the standard deviation of hourly values was $15\,\mathrm{W\,m^{-2}}$, which is equivalent to an uncertainty of one okta in the low cloud reports.

Upward longwave radiation was modelled by using $\epsilon\sigma T_s^4$ (ϵ is the emissivity of the sea surface, *ca.* 0.97, and σ is the Stefan–Boltzmann constant) and upward shortwave radiation by using atmospheric transmittance from Lumb's (1964) formulae in a model by Payne (1972).

2.6. *Sea surface temperature mapping* (SST)

SST measurements from *Tydeman* and R.R.S. *Challenger* during their surveys of the Hydrographic Survey Area have been combined with data from the corner ships and fixed moorings, and airborne radiation thermometer measurements (Liu & Katsaros 1983) to produce SST maps representative of a few days for three periods during JASIN: 4–10 August, 21–26 August and 27 August to 5 September. Care has been taken to remove data taken in periods of light winds and strong solar heating when the SST is likely to be unrepresentative of the mixed layer. Movement of features during the few days it takes for each survey (typically 25–50 km) leads to some distortion of the temperature fields. Nevertheless, Pollard (1982*a*) has shown that the resulting maps are consistent with the advective field imposed by predominantly geostrophic mesoscale eddies (Pollard 1982*b*) whose signal extends several hundred metres below the surface. SST features also exhibit similarities with the salinity distribution.

The technique of combining the measurements is quite accurate if the mixed-layer temperature (MLT) is assumed to be the same as the SST. The interface temperature, however, may differ from the MLT by as much as 0.5 K owing to radiation and evaporation. The SST maps that have been produced strictly represent the MLT rather than the actual interface temperature while the aircraft observations are essentially of the interface temperature. However, the radiometer, a

Barnes PRT5, is not accurate enough to resolve the differences between these two temperatures so the measured bulk temperatures from ships are used to calibrate the aircraft signal as well as possible. The interface temperature may be constructed locally from the surface energy balance and the algorithm developed by Liu *et al.* (1979). Besides the correction for drift the PRT5 measurement needs to be corrected for reflexion from the sky. This was obtained by using an upward-looking PRT6 to determine the sky temperature and an emittance value of the surface of 0.986 as suggested by Saunders (1970). The correction can be generalized for the C-130, which did not have an upward-looking radiometer but did measure the total longwave irradiance. However, in the present study only the Electra SST data are used.

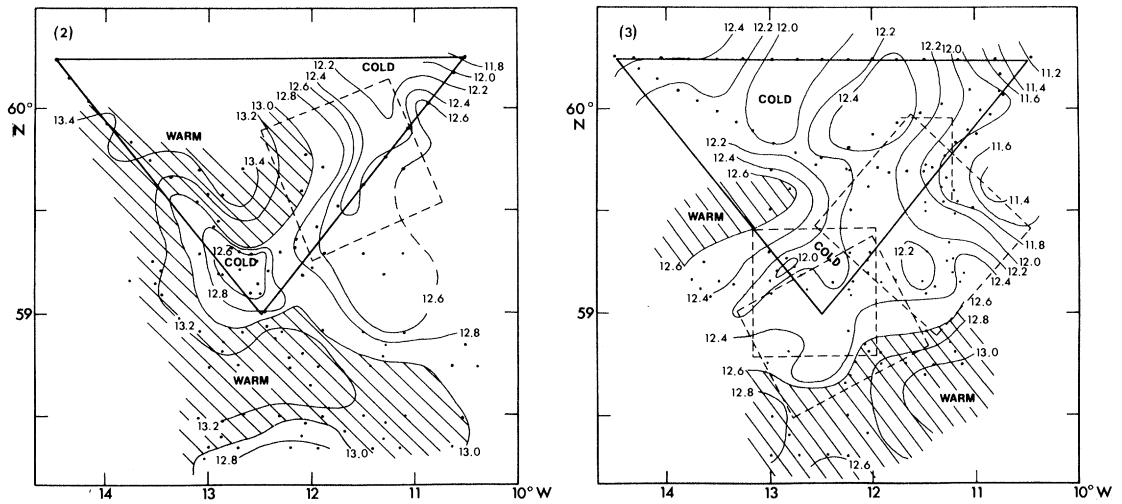

FIGURE 2. SST distribution (°C) from 4 to 10 August 1978. A composite of ship, buoy and aircraft measurements have been used and diurnal effects have been minimized. Dashed lines indicate areas of aircraft operation; locations of ship and buoy measurements are also shown.

FIGURE 3. SST distribution (°C) from 21 to 26 August.

3. General variability of fluxes and means

3.1. *Sea surface temperature distribution*

Taylor & Guymer (this symposium) have presented a map of the SST distribution of the northeast Atlantic (expressed in terms of equivalent potential temperature). Anomalously warm water at 50° N and 15° W provided a source of moist air above a warm front on 25 August. Horizontal gradients in the vicinity of JASIN were small according to this analysis based on sampling on scales of hundreds of kilometres. Using the data outlined in § 2.6 we have produced three SST maps, one in phase 1 (figure 2) and two in phase 2 (figures 3, 4), on which ocean scales of 20–200 km are resolved, i.e. resolution almost down to the frontal scale and encompassing the eddy scale.

Water to the south is persistently warmer at about 13 °C while in the northeast corner there is a sharp drop to below 11 °C. Hourly values at *Hecla* throughout the JASIN period show considerable variability between 10 °C and 12 °C, which also suggests a frontal region. Of particular interest is the presence of a cold tongue extending southwards in the east during phase 1, which appears to be caught up in a clockwise circulation, moving westwards along 59° N and then northwest as warm water moves eastward at 59.6° N during phase 2. These data are consistent with the position and motion of a mesoscale eddy moving west along 59.3° N as

described by Pollard (1982*a*) and can be identified with salinity features suggesting that the SST variations are not primarily due to diurnal effects in the top metre or so but are indicative of the advective field of the eddy. However, Pollard concludes that their structure probably does not extend below the mixed layer. Large east–west gradients exist near H2 (59° N, 12° 30′ W) in figure 4 and are the subject of a study by Minnett *et al.* (this symposium). Warm water in the northwest in phase 1 may be due to radiative effects in light wind conditions (see § 2.6).

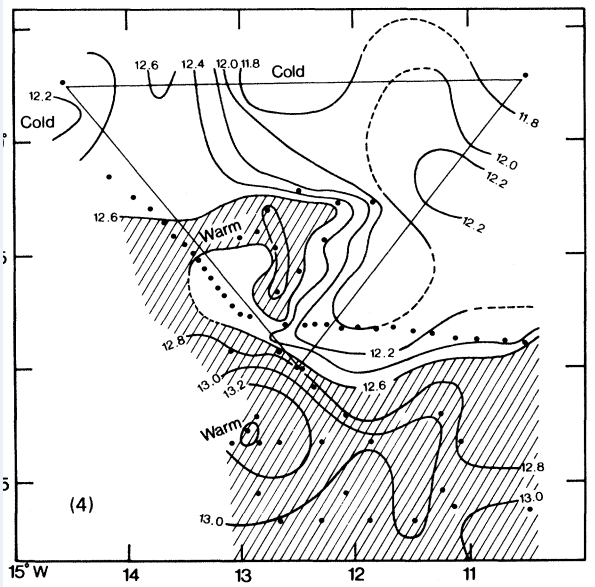

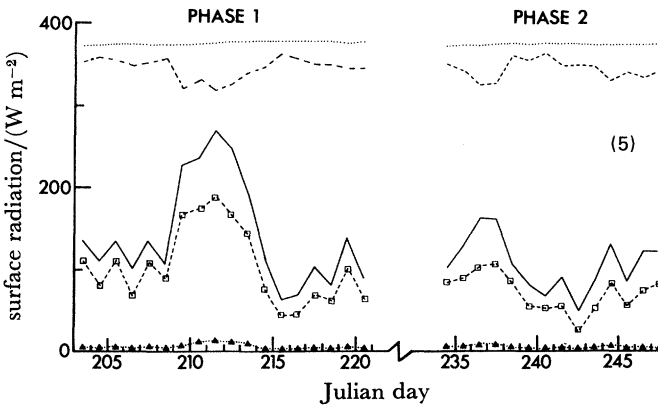

FIGURE 4. SST distribution (°C) from 27 August to 5 September. The Electra and C-130 flew three circuits of the 200 km triangle.

FIGURE 5. Daily mean values of the surface radiation components (dotted line, upward longwave; dashed line, downward longwave; solid line, downward shortwave; dashed line with squares, downward net radiation; dotted line with triangles, upward shortwave). Day 213 is 1 August; day 244 is 1 September. Note the break in the time axis between phases. Values shown are triangle means.

3.2. *Surface energy balance*

The heat balance at the ocean surface is given by

$$E_w = E_n - E_h - E_e, \tag{3}$$

where E_n is the net radiative flux (positive downwards), E_h and E_e are the sensible and latent heat fluxes and E_w is the heat that goes from the surface into the water.

Daily values of the radiation components during both phases are displayed in figure 5. Not surprisingly, given the rather small temporal changes in SST, the outging longwave radiation (LW) is nearly constant. Incoming LW is always smaller, especially around day 210 when skies were relatively clear. Incoming shortwave radiation (SW), which is strongly dependent on cloud cover, is very variable. SW(out) is mostly less than 10 W m^{-2} and is about 5 % of SW(in). The result is that the net radiative flux is always positive for daily means but varies between 20 and 190 W m^{-2}, larger values being obtained in phase 1.

An important question to ask is: how much of the net flux is available for heating the oceanic mixed layer? Mean latent heat fluxes at the corners of the meteorological triangle for each day

(figure 6) show a tendency to increase during phase 1, and a marked double peak in phase 2. This corresponds to a strong westerly flow bringing air from near Greenland, followed several days later by an incursion of some very dry air into the northeastern part of the triangle behind cold fronts as the track of disturbances became displaced further south (Pollard *et al.* this symposium). Generally, the sensible heat flux was very small, about 10 % of the latent heat flux apart from the second half of phase 1 when a northeasterly flow became established and brought in air from the cold water to the northeast of *Hecla*.

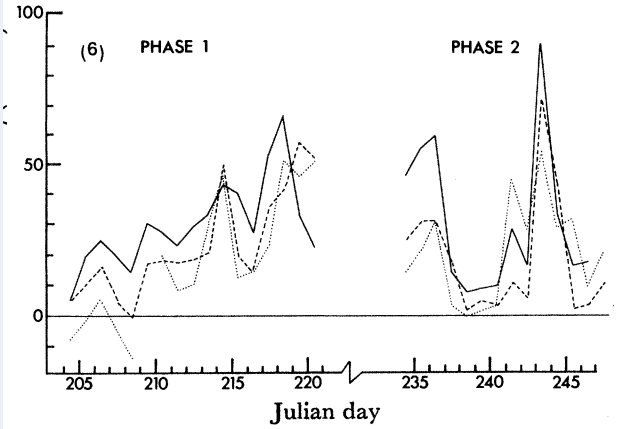

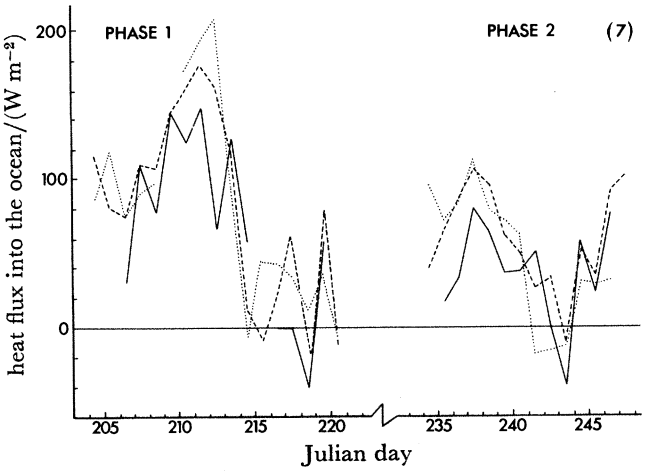

FIGURE 6. Daily mean values of the surface latent heat flux at the corners of the 200 km meteorological triangle (solid line, northwest corner; dashed line, south corner; dotted line, northeast corner).

FIGURE 7. Daily mean values of the heat flux into the ocean at the triangle corners calculated from equation 3 (solid line, northwest corner; dashed line, south corner; dotted line, northeast corner).

For JASIN the periods of relatively high turbulent fluxes were not correlated with high values of E_n. This results in large differences in the heat flux to the ocean, E_w, during the phases (figure 7). Towards the end of phase 1 the heating becomes rather small (cf. Prangsma *et al.* this symposium) and on two days (219 and 243) the latent heat flux was sufficiently large under cloudy skies to produce cooling. Prangsma *et al.* have compared this heat input to the ocean with the warming measured by CTD probes and have concluded that it accounts for nearly all the observed changes in the mixed layer temperature when averaged over horizontal scales larger than 90 km. Mean values of the terms in equation (3) are given in table 2. For comparison, mean values of E_h and E_e in GATE were more than twice those of JASIN (Seguin & Kidwell 1980).

By using figures 6 and 7 the daily mean values of E_e and E_w at each of the corners can be examined. Evaporation is generally lower in the south and combined with slightly higher values of E_n means that there is greater heat input to the ocean than at the other corners. Lowest values of E_w are to the northwest. However, it is interesting to note the increased heating on day 219, which combined with winds of 3 m s^{-1} (implying little vertical mixing beneath the surface) may account for the high values of SST recorded by *Tydeman* (figure 2), which was closest to this corner at the time. Mean values of E_n, E_h, E_e and E_w at each location are given for both phases in table 2.

Values of E_h and E_e have also been computed for *Tydeman*, *Discovery and Meteor* (dissipation);

for W2 and B4 only E_h has been obtained since no wet-bulb sensors were carried on these platforms. Results compare favourably with those of the corner ships. Results from W2, B4 and *Meteor* (dissipation) tend to be closest to those from *Meteor* (bulk).

3.3. *Temporal and spatial variation of surface stress*

Figure 8 describes the variation of τ_x and τ_y, the stress components, with time at each corner. A southwesterly flow at the beginning of phase 1 became northeasterly on day 214 with maximum values of 0.1 N m^{-2}. Large stresses of 0.15 N m^{-2} were found at the start of phase 2 in a westerly

TABLE 2. PHASE-MEAN FLUXES AT THE CORNERS OF THE METEOROLOGICAL TRIANGLE AND THEIR AREA MEANS: NET RADIATION (E_n), SENSIBLE HEAT (E_h), LATENT HEAT (E_e), HEAT FLUX FROM SURFACE INTO OCEAN (E_w), EASTWARDS (τ_x) AND NORTHWARDS (τ_y) MOMENTUM FLUX

(Phase 1 lasted from 23 July to 8 August; phase 2 lasted from 22 August to 4 September.)

	phase 1				phase 2			
	S	NW	NE	mean	S	NW	NE	mean
E_n/(W m^{-2})	109	108	101	106	79	70	67	72
E_h/(W m^{-2})	5	6	5	5	1	5	−1	2
E_e/(W m^{-2})	23	30	20	24	18	30	21	23
E_w/(W m^{-2})	81	72	76	76	60	35	47	47
E_h/E_e	0.22	0.21	0.24	0.22	0.05	0.16	−0.04	0.07
E_w/E_n	0.74	0.67	0.75	0.72	0.76	0.50	0.70	0.65
τ_x/(10^{-2} N m^{-2})	0.4	0.2	−1.9	−0.4	5.3	5.3	4.2	4.9
τ_y/(10^{-2} N m^{-2})	0.5	−0.3	0.3	0.2	−0.7	0.2	0	−0.2

flow and values again increased with the passage of a frontal system on day 242/243 as the flow backed southerly and then quickly veered. On the last day of this phase a strong east southeasterly wind developed ahead of an occlusion, the mixed-layer response to which has been studied by Pollard (this symposium). Mean values for each phase are given in table 2. Significant differences across the triangle occur on some days.

By using measurements of surface pressure and hourly mean observed winds at the triangle corners, daily mean values of cross-isobar flow angle (α) and the ratio of observed 10 m wind speed (V) to geostrophic speed (V_g) have been calculated and are also plotted in figure 8. Acceleration terms may still be significant in daily means especially when active fronts are close. These days are usually identifiable by the high standard deviations on the cross-isobar flow angle, σ_α. If days are selected on the basis of a steady and horizontally homogeneous flow then $V/V_g = 0.77$ and $\alpha = 11°$ compared with values found by Deacon (1973) of 0.77 and 17°. The wind-stress curl has been calculated for the 200 km triangle at hourly intervals and is expressed as a time series of daily mean vertical velocities (W) at the top of the friction layer (figure 9) where $W = 1/\rho f \times \text{curl } \boldsymbol{\tau}$ and is often called the Ekman pumping; f is the Coriolis parameter. Largest values (1 cm s^{-1}) occur near the beginning of phase 1 when depressions passed close by. Large downward motion is indicated behind the cold front late on 30 August (this is studied in greater detail in § 4) and on 5 August. The end of phase 1 is associated with downward motion. Large fluctuations are on a time scale of two to three days but higher frequency structure exists, which is resolved by the hourly values. If random errors on the individual winds of ± 1 m s^{-1} and ± 5° are assumed uncertainties in the daily mean W of ± 10 %, typically ± 0.1 cm s^{-1}, are implied.

For phase 2, values of W have also been calculated from the wind-stress curl obtained from a number of SASS passes. Stresses were interpolated on to a 50 km grid and $\partial\tau_y/\partial x$ and $\partial\tau_x/\partial y$

calculated over 100 km distances in 50 km steps. Although one estimate of W is a daily mean and the SASS samples over a few minutes the comparison between the two (figure 9) is encouraging and indicates that meaningful estimates of the curl can be obtained on the 100–1000 km scale. Fields of the Ekman pumping are discussed in the case studies of § 4. Vertical velocities have also been derived by integrating the divergence of boundary layer winds obtained by radiosondes from the corner ships (Taylor *et al.* this symposium). This shows that the total vertical velocity is

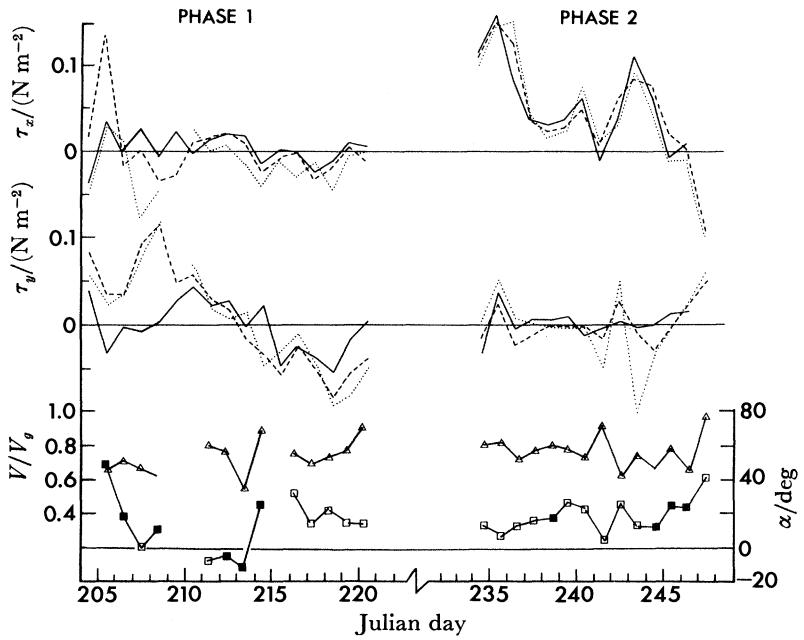

FIGURE 8. Upper, daily mean values of surface stress components (τ_x, τ_y) at the triangle corners calculated from equations (1) and (2) (solid line, northwest corner; dashed line, south corner; dotted line, northeast corner). Lower, daily mean values of the ratio of observed wind speed to geostrophic wind speed, V/V_g (triangles), and the cross-isobar flow angle, α (open squares, standard deviation of α, $\sigma_\alpha < 20°$; filled squares, $\sigma_\alpha > 20°$).

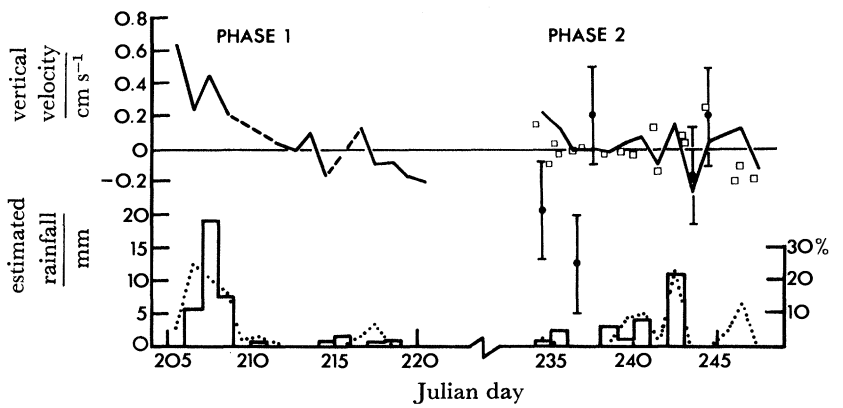

FIGURE 9. Upper, vertical velocity at the top of the atmospheric friction layer inferred from the curl of the wind stress (solid line, daily mean values obtained by using corner-ship WMO winds; squares, instantaneous values from scatterometer measurements). For comparison, mean vertical velocities for 15 h periods obtained by the divergence method applied to radiosonde boundary layer winds are shown (filled circles with error bars indicating the spread of four-hour estimates about the mean).

Lower, rainfall estimates (solid line, left-hand ordinate, daily accumulations derived from *Hecla* and *John Murray* rain-gauge data; dotted line, right-hand ordinate, percentage of hourly observations when rain was reported by the meteorological ships).

small and, given the uncertainties in the radiosonde estimates of ± 0.3 cm/s, implies that most of the observed W can be accounted for by Ekman pumping. In contrast, Weller (1982) has obtained a time series of the vertical motion just beneath the oceanic mixed layer based on heat budget considerations and, for a limited period, on vertical current meter measurements. Vertical velocities are at least ten times those that can be accounted for by Ekman pumping (metres per day compared with tenths of a metre per day).

The vertical motion in the atmosphere due to Ekman pumping has also been compared with rainfall measurements on *Hecla* and R.R.S. *John Murray*; daily accumulations are shown in figure 9. Since these are biased towards the northeast corner of the triangle, hourly WMO present-weather codes at all four meteorological ships have been analysed to give the percentage of occasions on each day when rain was reported. This shows similarities with the quantitative data. Rain tends to occur when the frictionally induced vertical motion is upward and this is especially true of the first few days of phase 1 and the end of phase 2.

4. Case studies

A three day period has been investigated in some detail to explore further horizontal variations in the turbulent fluxes and their relation to larger scales. The period chosen (30 August to 1 September) has been selected because it contains examples of the passage of a fairly well defined frontal system and mesoscale variations in a shallow convective boundary layer, both of which are sampled well by surface platforms, SASS and aircraft.

4.1. 30–31 *August*

During the evening of 30 August 1978 an occluding frontal system crossed the JASIN area. The warm front had made slow progress east but the cold front moved more rapidly towards eastsoutheast. Both fronts showed clearly on a NOAA-5 infrared picture at 20h30 G.M.T. and the warm sector was relatively cloud free.

Hourly bulk aerodynamic fluxes of momentum, sensible and latent heat have been calculated from the corner ships, *Tydeman* and *Discovery*, and buoy B4, with averaging where appropriate over the hour. Analysis of the measurements at the corners shows that the cold front was propagating at 8 m s^{-1} and moving towards 110°. This compares with values of 12 m s^{-1} and 100° calculated by Taylor *et al.* (1982) using the microwave radiometer on Seasat to track rain features. However, there is no *a priori* reason why the two should be the same. Rain-generating cells may be moving with a stronger wind at middle levels or even propagating relative to the wind at their level (Taylor & Guymer this symposium). Taylor *et al.* (1982) used their propagation velocity to turn hourly rain observations into spatial sections. A similar technique has been adopted in the present study for the turbulent fluxes. This is unlikely to be valid if the fluxes are dominated by local effects such as the variations in SST noted previously. Figures 10 and 11 show the sensible and latent heat flux distributions appropriate to 01h00 G.M.T. on 31 August just after the front passed through *Meteor*. Fluxes are small and negative ahead of the front but reverse sign behind, reaching maximum values 250–300 km further westnorthwest. A rather sharp gradient is observed in E_e about 100 km behind the surface cold front. This feature is generally front parallel except for pronounced minima in both E_h and E_e implied by the observations at the northeast corner, which may be due to the ship's entering colder water. Except in this region E_e is about seven to ten times E_h in unstable conditions.

PHILOSOPHICAL TRANSACTIONS OF THE ROYAL SOCIETY A MATHEMATICAL, PHYSICAL & ENGINEERING SCIENCES

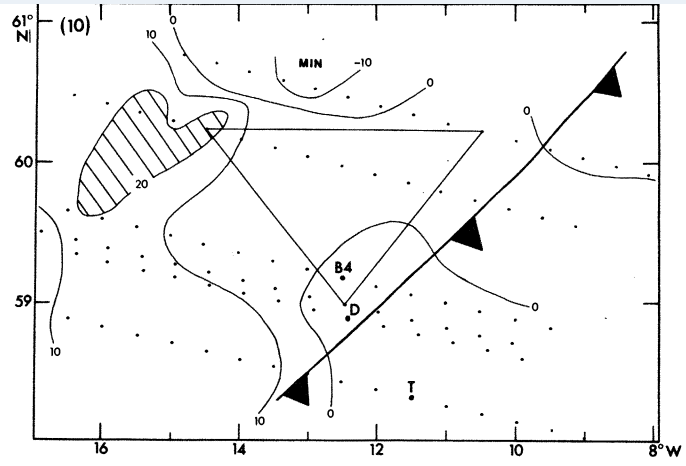

FIGURE 10. Horizontal variation of the surface sensible heat flux (E_h/(W m^{-2})), at 01h00 G.M.T. on 31 August 1978 obtained from hourly point measurements displaced according to the propagation speed of the cold front (8 m s^{-1}) towards 110°. Values more than 20 W m^{-2} are shown hatched. T, D and B4 are the positions of *Tydeman*, *Discovery* and buoy B4.

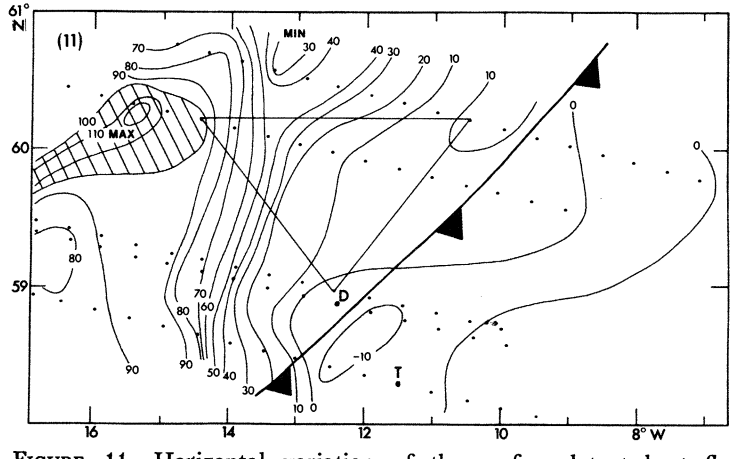

FIGURE 11. Horizontal variation of the surface latent heat flux (E_e/(W m^{-2})) at 01h00 G.M.T. on 31 August 1978 derived as in figure 10. Values more than 100 W m^{-2} are shown hatched.

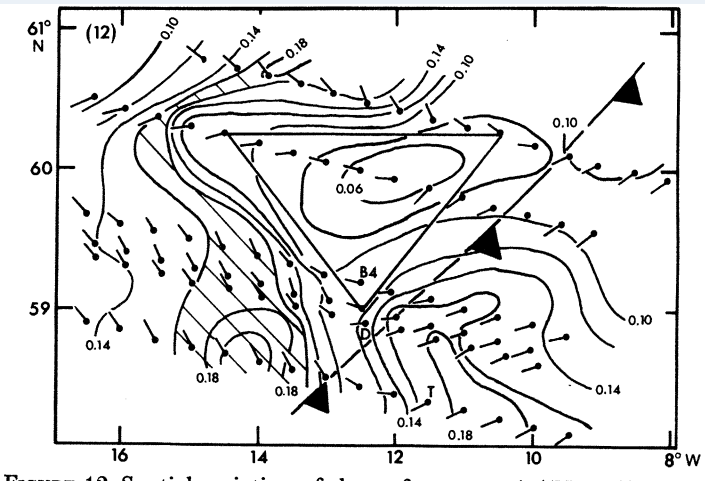

FIGURE 12. Spatial variation of the surface stress (τ/(N m^{-2})) at 01h00 G.M.T. on 31 August 1978 derived as in figure 10. Direction of stress indicated by —•; values more than 0.16 N m^{-2} are shown hatched.

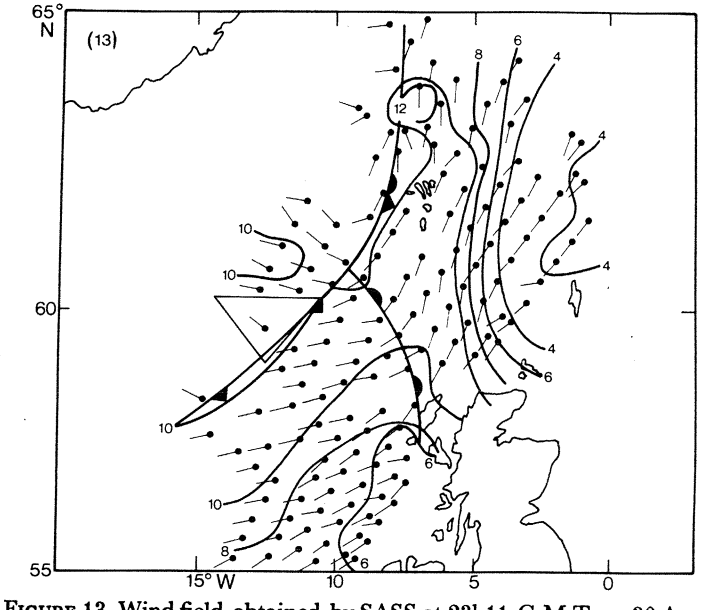

FIGURE 13. Wind field obtained by SASS at 23h11 G.M.T. on 30 August 1978 (wind speeds are in m s^{-1}; directions shown are those from which the wind is blowing). For clarity only every fifth data point is plotted.

The surface stress distribution is plotted similarly in figure 12. A pronounced veer in direction at or near the surface cold front is observed. Apart from this the most striking feature is the difference between the directions obtained by using measurements at the northwest corner and the rest. This results in the negative values of the wind-stress curl discussed in § 3. However, the magnitudes of the stress are reasonably well behaved over the area, with a zone of higher stress to the west and north of the Triangle. Considerable along-front variations also occur.

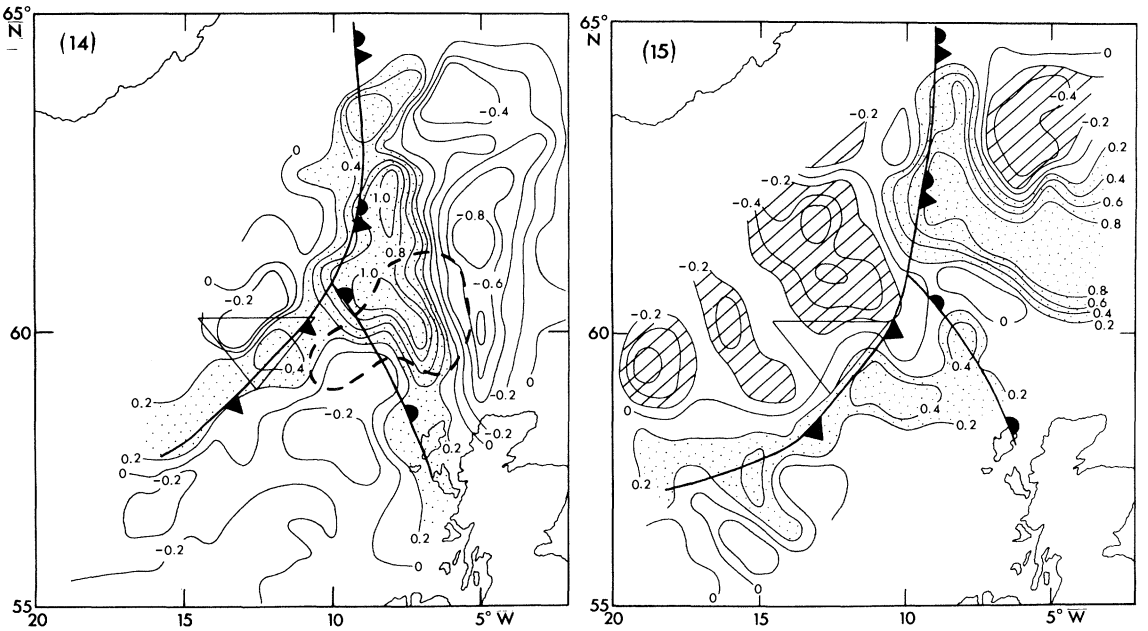

FIGURE 14. Vertical velocity (W/(m s^{-1})) distribution inferred from the curl of the wind stress at 23h11 G.M.T. on 30 August 1978. Values more than 2 cm s^{-1} are shown stippled; dashed line encloses a region where the Seasat microwave radiometer indicated rain rates exceeding 0.4 mm h^{-1}.

FIGURE 15. Vertical velocity (W/(m s^{-1})) at 00h50 G.M.T. on 31 August 1978. Values more than 0.2 cm s^{-1} are shown stippled, values less than 0.2 cm s^{-1} hatched.

We now examine the wind data from SASS on two consecutive passes close to midnight. Figure 13 shows the winds at 23h11 G.M.T. on 30 August; for clarity only every fifth solution has been plotted. Strong similarities with figure 12 are observed. A southerly flow occurs ahead of the warm front with westsouthwesterly winds in the warm sector, which veer to north of west behind the cold front. The wind change associated with the cold front occurs within 50 km and SASS can often be used to position surface fronts quite accurately. Winds are light several hundred kilometres ahead of the occlusion under a ridge and are strongest ahead of the surface fronts.

Figure 14 presents the distribution of vertical velocity inferred from the curl of the wind stress. Maximum magnitudes are 0.8–1.0 cm s^{-1} with greatest downward motion 200–300 km ahead of the occluded part of the front, i.e. to the west of the ridge axis. Upward motion occurs along or just ahead of the fronts especially near the occlusion point. Much of the warm-sector air is weakly descending. In general the pattern is consistent with the synoptic situation and agrees particularly well with the cloud distribution observed in the infrared. It may also be compared with maps of integrated water vapour, liquid water and rain rate produced for the same occasion by Taylor *et al.* (1982) from the Seasat microwave radiometer. Low values of water vapour were found in the

PHILOSOPHICAL TRANSACTIONS OF THE ROYAL SOCIETY A MATHEMATICAL, PHYSICAL & ENGINEERING SCIENCES

ridge, and the highest were in the warm air to the south of the meteorological triangle. The liquid-water maximum, however, was further northeast, near the occlusion, and coincides, of necessity owing to the nature of the algorithm used in processing the radiometer data, with the maximum rain rate of 0.8 mm h^{-1}. The rainfall distribution and intensity were shown to be consistent with WMO observations at the triangle corners and with rain-gauge measurements at *Hecla*. The area in which rain rate exceeded 0.4 mm h^{-1} is marked by the thick dashed line in figure 14 and lies close to maximum upward motion.

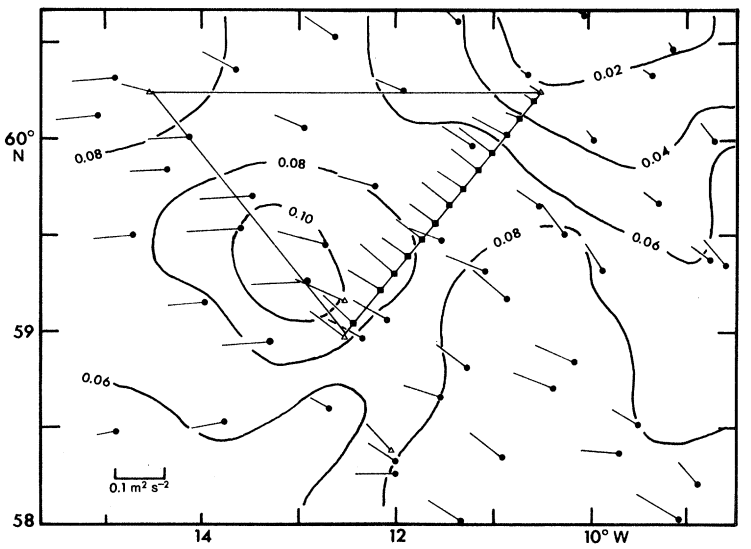

FIGURE 16. Spatial variation of u_*^2 on 1 September determined from the scatterometer at 06h52 G.M.T. (circles), from Electra at 06h40–07h10 G.M.T. (squares) and from ships and buoys at 07h00 G.M.T. (triangles).

Such data imply that warm, moist air ahead of the cold front is being lifted and some of the water vapour is being converted to liquid water as it moves towards the occlusion point. Here it experiences additional uplift and rain is produced. Thus there appears to be a strong link between boundary layer convergence and the dynamics of the middle troposphere.

The vertical velocity pattern on the next satellite pass, in which coverage is obtained of a larger area behind the cold front, is presented in figure 15. Weak motion along the cold front is still occurring. However, the area of maximum motion has moved rapidly northeast (propagation speed *ca.* 30 m s^{-1}) ahead of the warm front and has adopted an east–west orientation. An interesting feature is the banded structure appearing in the cold air with a spacing of about 200 km. Later, on 31 August, NOAA-5 visible images showed mesoscale organization of the stratocumulus over the JASIN area, which may be related to these structures. It should also be noted that a line joining the regions of maximum downward motion passes very close to the region of maximum latent heat flux (figure 11).

4.2. 1 *September*

On 1 September the JASIN area was still in the cold air behind the fronts of 30–31 August (§ 4.1). However, the cold front returned as a warm front from the southwest and affected the triangle late in the day, passing through *Endurer's* position at 18h00 G.M.T. Ahead of it the flow was westerly to northwesterly. From 06h00 to 08h00 G.M.T., when the Electra made two complete circuits of the triangle, the northern part of the area was relatively cloud-free with lines

of cumulus evident on visible satellite imagery. There was some indication that the lines of cumulus became more developed to the east, possibly forming cumulonimbus. Further south more extensive stratocumulus was observed with middle-level cloud in a band lying WNW–ESE.

As the Electra proceeded northeast from the southern corner, clouds became predominantly cumulus with large regions of clear sky between. The westward leg from *Hecla* to *Endurer* was characterized by the presence of several cloud lines oriented at an acute angle to the flight path and approximately parallel to the surface wind. The final leg showed little evidence of these

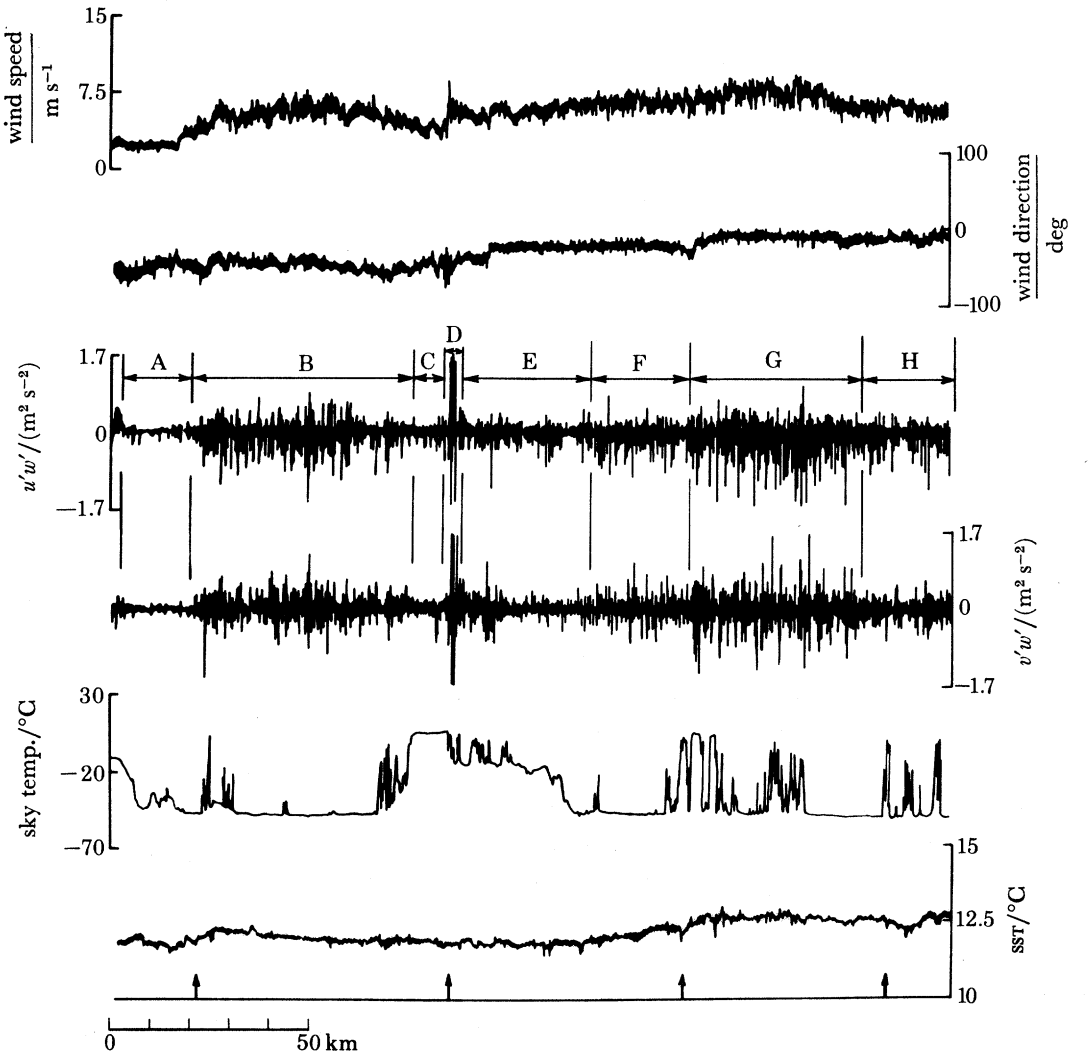

FIGURE 17. Wind speed and direction, along-wind ($u'w'$) and cross-wind ($v'w'$) instantaneous momentum flux and SST measured by the Electra while flying from the northeast to the northwest corner of the 200 km triangle on 1 September. SST has been corrected for cloud effects by using the upward-looking PRT-6 data. The wind direction is relative to the mean wind direction over the whole triangle. Arrows at the bottom of the figure mark lines of cumulus observed from the aircraft. Mean stress, τ, and direction towards which it is acting, θ, (i.e. opposite to that from which wind is blowing) for the regions A–H indicated above the $u'w'$ trace are as follows:

	A	B	C	D	E	F	G	H
$10^2(\tau/\rho)/(\mathrm{m^2\ s^{-2}})$	0.51	4.0	2.8	7.3	2.7	4.3	8.7	4.9
θ/deg	155	137	145	−1.4	144	144	158	159

cloud lines, the boundary layer being capped primarily by stratus and stratocumulus. Similar features were observed on the second circuit of the triangle, which was the reverse of the first.

During these flights SASS coverage was obtained on two consecutive Seasat passes. Figure 16 shows u_*^2 from SASS and surface data together with eddy correlation measurements from the Electra for that leg of the triangle during which the first Seasat pass occurred. Agreement is good

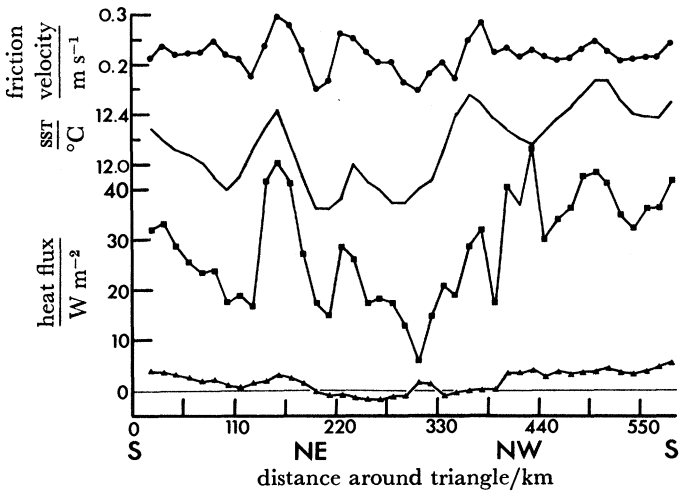

FIGURE 18. Variations in turbulent fluxes measured by the C-130 at a height of 50 m as it flew round the 200 km JASIN triangle on the afternoon of 1 September (circles, friction velocity; squares, latent heat flux; triangles, sensible heat flux). SST measured by the Electra is also shown.

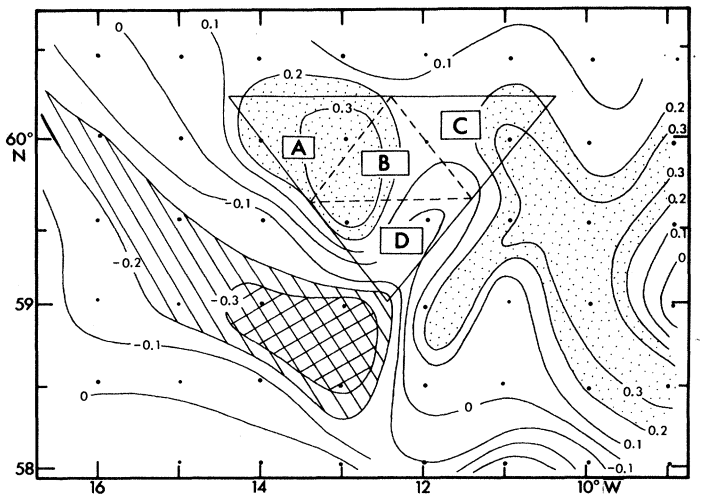

FIGURE 19. Vertical velocity (W/(cm s^{-1})) distribution inferred from the curl of the scatterometer wind stress at 06h52 G.M.T. on 1 September. Values for upward motion at more than 0.2 cm s^{-1} are shown stippled; for downward motion at more than 0.2 cm s^{-1} hatched, and for downward motion at more than 0.3 cm s^{-1} cross-hatched.

for both magnitude and direction and the general trend is for the stress to decrease towards the northeast. However, the agreement is poorer by the time the aircraft flies the remaining legs, which take $\frac{1}{2}$ h each. On the next SASS pass agreement was again obtained for measurements less than $\frac{1}{4}$ h apart (this time on the southwest side of the triangle) but this deteriorated as the time difference increased. It would appear that significant changes were occurring on the sub-200 km scale and on time scales of an hour.

PHILOSOPHICAL TRANSACTIONS OF THE ROYAL SOCIETY A MATHEMATICAL, PHYSICAL & ENGINEERING SCIENCES

Of particular interest are the stress variations along the northern leg (figure 17). The distinctive feature is the grouping into regions 50 km in length of relatively large and small turbulent fluctuations, which appear to be related to low frequency variations in SST. It is of interest that the cloud lines (the width of which is much smaller than 50 km) occur close to the transitions from one stress region to another. This is clearly evident for the cloud line on the left of the figure, which marks the change from the stress minimum in the northeast corner ($\tau/\rho = 5.1 \times 10^{-3}$ $m^2 s^{-2}$) to a region where it is nearly an order of magnitude larger (4.0×10^{-2} $m^2 s^{-2}$). The largest change of stress, in the middle of the leg, was associated with a very large horizontal wind shear and occurred in the vicinity of an oceanic front (figure 4). An infrared satellite picture showed the convective cloud at this position to be significantly deeper.

TABLE 3. COMPARISON OF VERTICAL VELOCITIES/(CM S^{-1}) ON 1 SEPTEMBER RESULTING FROM EKMAN PUMPING CALCULATED BY USING ELECTRA, C-130 AND SASS STRESS DISTRIBUTIONS FOR THE FOUR SUB-TRIANGLES SHOWN IN FIGURE 19. THE 12 HOUR, TRIANGLE-MEAN VERTICAL VELOCITY AT THE TOP OF THE FRICTION LAYER DEDUCED FROM THE INTEGRATED DIVERGENCE OF RADIOSONDE WINDS (RS) IS ALSO GIVEN

	period (G.M.T.)	sub-triangle A	B	C	D	whole triangle
Electra	06h40–08h16	0.39	−0.05	0.46	−0.24	0.27
Electra	08h27–10h06	0.55	0.57	0.20	0.16	0.18
C-130	13h30–16h08	0.17	0.29	−0.07	−0.38	−0.17
SASS	06h50	0.31	0.22	0.25	0.07	0.21
SASS	08h28	−0.04	0.05	0.36	−0.16	0.05
RS	06h00–18h00	—	—	—	—	0.12

A few hours later the C-130 flew around the triangle at 50 m and the along-track variability of u_*, E_h, and E_e is shown in figure 18 with SST from the Electra flights. In this case 12 km averages have been plotted. All the fluxes show variations on scales of a few tens of kilometres that are related to similar variations in the underlying SST, particularly near the northeast corner where warm water is associated with higher values of u_* and E_e. The sensible heat flux is small, especially on the northern leg.

Values of vertical velocity due to Ekman pumping have been deduced by using SASS and aircraft data. Figure 19 shows its horizontal distribution on Rev. 948, where descent to the southwest is associated with a ridge ahead of the advancing warm front and coincides with low values of integrated water vapour from the Seasat microwave radiometer. Upward motion to the east of the area is close to where cumulus were observed to be developing into cumulonimbus. Mesoscale activity is again observed. Values of W were also calculated for the 200 km triangle and the four sub-triangles shown in figure 19 by using the aircraft stresses and are compared with SASS estimates in table 3. In all cases upward motion is weaker in the southern sub-triangle. It should be remembered that the aircraft take some time to cover the three corners of each triangle, especially B and D, so that the comparisons are limited. Table 3 also gives W calculated from the divergence of the radiosonde winds averaged over the large triangle and 12 h. This value, 0.12 ± 0.3 cm s^{-1}, compares very well with the corresponding mean of the aircraft flights, 0.09 ± 0.2 cm s^{-1}.

From these observations it is clear that the stress field over the ocean is highly variable in the horizontal on a scale of 50 km despite the topographical uniformity of the sea surface. Further-

more, there is a suggestion that this is closely associated with changes in SST, which can cause the stratification to switch between being unstable and stable under conditions of overall near-neutral stability. This also affects the Ekman pumping on the mesoscale. Since near-neutral conditions prevail for much of the time in the mid-latitude, marine boundary layer during summer this horizontal variability in the fluxes is likely to be common.

5. Summary

Surface turbulent fluxes and SST have been examined on scales from several kilometres to 200 km and for days to weeks by using a combination of ships, buoys, aircraft and microwave remote sensing. The net radiative flux had been obtained at the corners of the 200 km meteorological triangle either by direct measurements of the shortwave and longwave components or by parametrization techniques. This has enabled the surface heat budget to be examined on a daily basis. About 70 % of the net flux (typically 100 W m^{-2} in phase 1 and 70 W m^{-2} in phase 2) is available for heating the ocean and, of the remainder, over 75 % goes into the atmosphere as latent heat. In these near-neutral conditions the mean surface wind speed across the triangle was 77 % of the geostrophic wind speed and the cross-isobar flow angle was 11° (down-gradient).

Significant variations in the thermodynamic fluxes across the area were found, associated partly with the SST distribution and also with the fact that the coldest and driest air was limited to the northern part of the triangle by the synoptic situations. There were also systematic differences in the stress. The curl of the wind stress was evaluated and a time series of the Ekman pumping constructed. Variations were consistent with events on the synoptic scale and especially with rainfall observations.

Case studies for a three-day period enabled a more detailed study to be made of the spatial distribution of the fluxes across and behind a well developed frontal system. Stresses derived from a satellite-borne scatterometer were used to investigate the Ekman pumping on scales from 50 km to several hundred kilometres and showed evidence of mesoscale variations. Some evidence for the modulation of surface momentum and moisture fluxes by mesoscale SST variations has been provided by aircraft data. Nicholls *et al.* (this symposium) suggest that mixing processes between the top of the Ekman layer and the inversion marking the top of the boundary layer occur intermittently and account for differences between the radiosonde budget results (Taylor *et al.* this symposium) and the direct flux measurements of the aircraft. SST variability on the mesoscale is one possible cause of such intermittency, especially in near-neutral conditions. The SST pattern itself has been strongly affected by the presence of a 100 km oceanic eddy. Thus, it is possible to identify one way in which oceanic features beneath the mixed layer could affect transfers through the atmospheric boundary layer, and, in consequence, larger-scale meteorological processes.

Further work is necessary on the possible sea-state dependence of the surface wind measurements and the implications for estimating near-surface winds from backscatter measurements. The data set will also be useful for examining the variation of fluxes on shorter time and space scales, including possible diurnal effects.

PHILOSOPHICAL TRANSACTIONS OF THE ROYAL SOCIETY A MATHEMATICAL, PHYSICAL & ENGINEERING SCIENCES

References

Born, G. H., Lame, D. B. & Rygh, P. J. 1981 A survey of goals and accomplishments of the Seasat mission. In *Oceanography from space*, pp. 3–14. New York: Plenum.

Bracalente, E. M., Boggs, D. H., Grantham, W. L. & Sweet, J. L. 1980 The SASS scattering coefficient σ^0 algorithm. *IEEE J. oceanic Engng*, OE**5**, 145–154.

Deacon, E. L. 1973 Geostrophic drag coefficients. *Bound. Layer Met.* **5**, 321–340.

Deardorff, J. W. 1968 Dependence of air–sea transfer coefficients on bulk stability. *J. geophys. Res.* **73**, 2549–2557.

Friehe, C. A. & Schmitt, K. F. 1976 Parametrization of air–sea interface fluxes of sensible heat and moisture by bulk aerodynamic formulae. *J. phys. Oceanogr.* **6**, 801–809.

Garratt, J. R. 1977 Review of drag coefficients over ocean and continents. *Mon. Weath. Rev.* **105** 115–129.

Grantham, W. L., Bracalente, E. M., Jones, W. L. & Johnson, J. W. 1977 The seasat-A satellite scatterometer. *IEEE J. oceanic Engng*, OE**2**, 200–206.

Guymer, T. H. 1983 JASIN 1978 surface meteorological data. IOS internal report. (In preparation.)

Guymer, T. H., Businger, J. A., Jones, W. L. & Stewart, R. H. 1981 Anomalous wind estimates from the Seasat scatterometer. *Nature, Lond.* **294**, 737–739.

Holland, J. Z. 1973 A statistical method for analyzing wave shapes and phase relationships of fluctuating geophysical variables. *J. phys. Oceanogr.* **3**, 139–155.

Johnson, J. W., Williams, Jr, L. A., Bracalente, E. M., Beck, F. B. & Grantham, W. L. 1980 Seasat-A satellite scatterometer instrument evaluation. *IEEE J. oceanic Engng* OE**5**, 138–144.

Jones, W. L., Boggs, D. H., Bracalente, E. M., Brown, R. A., Guymer, T. H., Chelton, D. & Schroeder, L. C. 1981 Evaluation of the Seasat wind scatterometer. *Nature, Lond.* **294**, 704–707.

Kondo, J. 1975 Air–sea bulk transfer coefficients in diabatic conditions *Bound. Layer Met.* **9**, 91–112.

Large, W. G. 1979 The turbulent fluxes of momentum and sensible heat over the open sea during moderate to strong winds. Ph.D. thesis, Institute of Oceanography and Department of Physics, University of British Columbia (180 pp.).

Large, W. G. & Pond, S. 1982 Sensible and latent heat flux measurements over the ocean. *J. phys. Oceanogr.* **12**, 464–482.

Lenschow, D. 1970 Airplane measurement of planetary boundary layer structure. *J. appl. Met.* **9**, 874–884.

Lind, R. J. & Katsaros, K. B. 1982 A model of longwave irradiance for use with surface observations. *J. appl. Met.* (In the press.)

Lind, R. J., Katsaros, K. B. & Gube, M. 1983 Measurement of short and longwave radiation components during JASIN 1978 and their parameterization. *J. appl. Met.* (In preparation.)

Liu, W. T., Katsaros, K. B. & Businger, J. A. 1979 Bulk parameterization of air–sea exchanges of heat and water vapour including the molecular constraints at the interface. *J. atmos. Sci* **36**, 1722–1735.

Liu, W. T. & Large, W. G. 1981 Determination of surface stress by Seasat–SASS: A case study with JASIN data. *J. phys. Oceanogr.* **11**, 1603–1611.

Liu, W. T. & Katsaros, K. B. 1983 Mesoscale variations of sea surface and air temperatures as measured on an airplane during JASIN. *J. geophys. Res.* (In preparation.)

Lumb, F. E. 1964 The influence of cloud on hourly amounts of total solar radiation at the sea surface. *Q. Jl R. met. Soc.* **90**, 43–56.

Nicholls, S. 1978 Measurement of turbulence by an instrumental aircraft in a convective atmospheric boundary layer over the sea. *Q. Jl R. met. Soc.* **104**, 653–676.

Nicholls, S., Shaw, W. J. & Hauf, T. 1983 An intercomparison of aircraft turbulence measurements made during JASIN. *J. appl. Met.* (To be submitted.)

Payne, R. E. 1972 Albedo of the sea surface. *J. Atmos. Sci.* **29**, 959–970.

Pollard, R. T. 1982*a* Eddies and fronts in the JASIN area. JASIN news, no. 25.

Pollard, R. T. 1982*b* Mesoscale (50–100 km) circulations revealed by inverse and classical analysis of the JASIN hydrographic data. *J. phys. Oceanogr.* (Submitted.)

Pond, S., Large, W. G., Miyake, M. & Burling, R. W. 1979 A Gill twin propeller-vane anemometer for flux measurements during moderate and strong winds. *Bound. Layer Met.* **16**, 351–364.

Saunders, P. M. 1970 Corrections for airborne radiation thermometry. *J. geophys. Res.* **75**, 7596–7601.

Seguin, W. R. & Kidwell, K. B. 1980 Influence of synoptic scale disturbances on surface fluxes of latent and sensible heat. *Deep-Sea Res.* **26** (GATE suppl. I), 51–64.

Taylor, P. K., Guymer, T. H., Katsaros, K. B. & Lipes, R. G. 1982 Atmospheric water distributions determined by the Seasat multichannel microwave radiometer. In Proc. Symp. *Variations in the Global Water Budget*, Oxford, 10–15 August, 1981. (In the press.)

Weller, R. A. 1982 The relation of near-inertial motions observed in the mixed-layer during the JASIN (1978) experiment to the local wind stress and the quasi-geostrophic flow field. *J. phys. Oceanogr.* **12**, 1122–1136.

Weller, R. A., Payne, R. E., Large, W. G. & Zenk, W. 1983 Wind measurements from oceanographic moorings. *J. appl. Met.* (To be submitted.)

PHILOSOPHICAL TRANSACTIONS OF THE ROYAL SOCIETY A MATHEMATICAL, PHYSICAL & ENGINEERING SCIENCES

Discussion

J. G. Harvey (*University of East Anglia, Norwich, U.K.*). What was the source of the precipitation data that were presented, and is there any possibility of obtaining precipitation estimates throughout the period of the project to be used with evaporation data to compute water budgets for the upper ocean?

T. H. Guymer. Primarily rain-gauge data from *Hecla* and *John Murray* were used but on one occasion estimates were made from data from the Seasat microwave radiometer. The latter, which are instantaneous values, are only obtained at best once per day but it may be possible to infer daily rainfall accumulations at a point if the steady-state assumption applies. This would also help in periods when ships were off station. It should be noted that ship-borne measurements of precipitation tend to be unreliable because of flow distortion effects. Nevertheless, we are attempting to estimate the evaporation minus precipitation term and preliminary work suggests that on average 1 mm day^{-1} was evaporated from the surface and 1–2 mm day^{-1} was precipitated during JASIN.

R. T. Pollard (*Institute of Oceanographic Sciences, Brook Road, Wormley, Godalming, Surrey GU8 5UB, U.K.*). Dr Guymer argued that changes in sea surface temperature cause changes in latent heat flux. Could drier air have caused the changes?

T. H. Guymer. Examination of the specific humidity of the air (q_a) from the C-130 flight showed that fluctuations were of about the same magnitude (0.5 g kg^{-1}) as those in the saturation specific humidity at the sea surface. However, they were not well correlated with the latent heat flux calculated from the eddy correlation measurements and appeared to be on a larger scale. Possibly, the variations in q_a themselves reflect the recent passage of the air over SST changes upwind. We are investigating the implication of these results for the bulk parametrization of the fluxes.

PHILOSOPHICAL TRANSACTIONS OF THE ROYAL SOCIETY A MATHEMATICAL, PHYSICAL & ENGINEERING SCIENCES